

**Panjawat Kongsuwan**  
Graduate Student  
e-mail: pk2261@columbia.edu

**Gen Satoh**  
Research Assistant  
e-mail: gs2358@columbia.edu

Department of Mechanical Engineering,  
Columbia University,  
New York, NY 10027

**Y. Lawrence Yao**  
Professor  
Manufacturing Research Laboratory,  
Department of Mechanical Engineering,  
Columbia University,  
New York, NY 10027  
e-mail: yly1@columbia.edu

# Transmission Welding of Glass by Femtosecond Laser: Mechanism and Fracture Strength

*Femtosecond laser pulses were focused on the interface of two glass specimens. Proper use of optical and laser processing parameters enables transmission welding. The morphology of the weld cross section was studied using differential interference contrast optical microscopy. In addition, a numerical model was developed to predict the absorption volumes of femtosecond laser pulses inside a transparent material. The model takes into account the temporal and spatial characteristics and propagation properties of the laser beam, and the transmission welding widths were subsequently compared with the absorption widths predicted by the model. The model can lead to the achievement of a desirable weld shape through understanding the effects of laser pulse energy and numerical aperture on the shape of the absorption volume. The changes in mechanical properties of the weld seams were studied through spatially resolved nanoindentation, and indentation fracture analysis was used to investigate the strength of the weld seams.*

[DOI: 10.1115/1.4005306]

## 1 Introduction

Glasses are widely used in various flat panel displays and biomedical applications. Joining techniques of glasses are usually based on the use of an adhesive agent or interlayer. Laser beam welding is considered to be a highly flexible technique with potential for joining glasses. The main advantages of laser welding over processes such as adhesive joining and anodic bonding are that the energy is supplied without physical contact to the workpiece and can be selectively coupled to the desired joining area, respectively. Due to the high level of transmission of light through transparent materials, glass-glass joining by conventional lasers requires an interlayer or opaque material between the top and bottom pieces to absorb the laser energy. Due to the nonlinear absorption characteristics of femtosecond lasers, however, transmission welding of transparent materials without an interlayer is possible when the laser beam is tightly focused on the interface.

Two different regimes of transmission welding by ultrashort pulsed lasers have been identified. Welding in the low repetition rate regime (1–200 kHz) and high repetition rate regime (>200 kHz) is dependent on whether the time interval between successive pulses is longer or shorter than the characteristic time for heat diffusion outside the focal volume [1]. Tamaki et al. [2] first demonstrated welding between two silica glass plates without a light-absorbent intermediate layer using a low repetition rate femtosecond laser. Watanabe et al. [3] then reported the welding of dissimilar transparent materials using the same femtosecond laser, and also investigated the parameters that resulted in joining by varying the laser pulse energy and the translation velocity. To this point, however, there have been no. morphological studies of the weld seam and the geometry of the weld in this low repetition rate regime is not well understood. Tamaki et al. [4] also reported on laser microwelding of transparent materials based on a localized heat accumulation effect using high repetition rate femtosecond laser irradiation and performed a simple tensile test after welding to estimate the joint strength. The testing procedure, how-

ever, was not precise due to its inability to continuously increase the applied load. Further studies [5–7] on the possibility of ultrashort pulsed laser welding of borosilicate glass substrates in the high repetition rate regime have been reported; however, there has been no. quantitative evaluation of joint strength and no. studies on the mechanical properties of the weld seam.

There are many attempts to simplify the problem by characterizing mechanical properties of the molten region irradiated by an ultrashort pulse laser inside a single-piece of transparent material. Miyamoto et al. [8] evaluated the mechanical strength of the laser-melt zone using a three-point bending test, and showed that the strength in that zone was as high as in the unirradiated base material; however, the sample had to be polished to locate the laser induced feature on the bottom surface of the test sample in order to maximize the tensile strength. Borrelli et al. [9] performed a double torsion test to measure fracture toughness, and revealed that the apparent fracture toughness is increased within the laser-treated area. Bellouard et al. [10] used nanoindentation tests to show an increase in Young's modulus within the laser-treated zones of fused silica irradiated by femtosecond pulses with high repetition rate; however, these measurements were not constrained to within the treated regions. Kongsuwan et al. [11] performed spatially resolved nanoindentation tests and revealed a decrease in Young's Modulus and hardness, and an increase in ductility in regions of fused silica irradiated by femtosecond laser pulses with low repetition rate. The mechanical properties and strength of real weld seams rather than of features created inside single-piece specimen, however, still requires further investigation.

In this study, transmission welding using a femtosecond laser at a low repetition rate has been performed to investigate the morphology and mechanical properties of the weld zone. The role and effect of the gap at the interface between two transparent material plates on the welding and joining mechanisms have also been investigated. Differential interference contrast optical microscopy is employed to study the morphology of the weld cross section, and a numerical model is developed to predict the feature shape. The possibility of using the absorption volume predicted by the model as a guideline for selecting processing parameters to get a desirable weld shape is also discussed. Spatially resolved

Contributed by the Manufacturing Science Division of ASME for publication in the JOURNAL OF MANUFACTURING SCIENCE AND ENGINEERING. Manuscript received April 1, 2011; final manuscript received September 30, 2011; published online January 11, 2012. Assoc. Editor: Yong Huang.

nanindentation is used to investigate the changes in mechanical properties, and indentation fracture analysis is performed to study the strength of the material in the weld seams.

## 2 Background

**2.1 Formation Mechanism of Transmission Welding by Femtosecond Laser.** When a femtosecond laser beam is tightly focused by objective lens on the interface of two transparent material plates, the laser intensity at a focal region becomes extremely high resulting in nonlinear absorption. Due to the Gaussian temporal profile of a femtosecond laser pulse, the leading edge of the converging laser pulse starts breakdown the material at or above the focal plane when the intensity reaches the material ionization threshold, and the subsequent portions of the laser pulse with higher intensity then produce breakdown still further above the focal plane where the beam diameter is larger [12,13] leading to a teardrop-shaped absorption volume.

At the end of the femtosecond laser pulse, the laser energy absorption process is completed, and a hot-electron plasma will be almost completely confined within the absorption volume with its surface area partially exposed to the air gap inevitably existing between the two plates. When the electrons have transferred their energy to the ions of the material, hydrodynamic motion starts, and a shock wave emerges from the energy deposition zone [14]. The average pressure,  $P_{avg}$ , in the absorption volume,  $V_{abs}$ , that drives the shock wave can be calculated as [15]

$$P_{avg} \approx Q_{dep} = \frac{AE_p}{V_{abs}} \quad (1)$$

where  $Q_{dep}$  is the total deposited energy density,  $A$  is the absorption coefficient, and  $E_p$  is the laser pulse energy. When two parallel transparent material plates are pressed together to have a very small gap, the van der Waals force per unit area,  $F_{vdw}$ , between the two plates is given by [16]

$$F_{vdw} = \frac{0.162hc}{d^4\pi^3} \left( \frac{n_\infty^2 - 1}{n_\infty^2 + 2} \right)^2 \quad (2)$$

where  $d$  is the distance between plates,  $h$  is the Planck's constant,  $c$  is the speed of light, and  $n_\infty$  is the refractive index of the plates at infinite wavelength. The shock pressure in the absorption volume due to ultrafast laser processing is considerably higher than the van der Waals force per unit area between the two plates. Considering model of a beam simply supported at both ends and subjected to a concentrated load at any point [17], the gap at the interface is increased by a deflection,  $\delta$ , which can be written as

$$\delta = \frac{2[(P_{avg} - F_{vdw})\pi w_{xy}^2]ba(l^2 - a^2 - b^2)}{6EI} \quad (3)$$

where  $w_{xy}$  is the radius of the absorption volume,  $l$  is the distance between both supported ends,  $a$  and  $b$  are the distance from the load point to each supported end,  $E$  is the Young's modulus of the material, and  $I$  is the area moment of inertia. This deflection is approximated from the average pressure in Eq. (1) which is a simplified model with a linear relationship to energy density. However, the pressure inside the absorption volume could be a nonlinear function of energy density due to phase transition. After the femtosecond laser absorption process, the free electrons and the lattice will attain a local thermodynamic equilibrium in a time scale on the order of picoseconds [15] after which the materials will be in a superheated state [18]. In addition to shock wave emission, the absorption volume will undergo a thermal process in which phase transitions take place. For high levels of superheating, corresponding to high excitation energy density, nucleation of gas bubbles or phase explosion can occur, and a heterogeneous

phase of vapor and liquid droplets may develop [19,20]. The nucleation of gas bubbles causes an increase in the pressure within the absorption volume [20]. This could result in greater deflection of the plates and possible ejection of the material [20,21].

**2.2 Numerical Analysis of Absorption Volume.** Based on the fundamentals of laser beams and optics, in order to accurately capture the shape of the absorption volume, a numerical model should be constructed by considering the Gaussian temporal distribution of laser power,  $P(t)$ , within the laser pulse duration as given in Eq. (4) as well as the Gaussian spatial distribution of the laser intensity,  $I(x, y, t)$ , as given in Eq. (5).

$$P(t) = \frac{E_p\sqrt{4\ln 2}}{\sqrt{\pi}t_p} \exp\left[-4\ln 2\left(\frac{t-2t_p}{t_p}\right)^2\right] \quad (4)$$

$$I(x, y, t) = \frac{2P(t)}{\pi R_0^2} \exp\left[-\frac{2r^2}{R_0^2}\right] \quad (5)$$

where  $E_p$  is the laser pulse energy,  $t_p$  is pulse duration,  $r = \sqrt{x^2 + y^2}$  is the distance from the center of laser beam,  $R_0$  is the  $1/e^2$  radius of the unfocused beam, and  $t$  is time. A laser beam with an intensity profile corresponding to Eq. (5) will converge to a diffraction-limited spot radius,  $w_0$ , and the beam waist as a function of distance from the focal plane,  $w(z)$ , can be calculated as

$$w(z) = w_0 \left[ 1 + \left( \frac{\theta z}{w_0} \right)^2 \right]^{1/2}; \quad w_0 = \frac{M^2\lambda}{\pi NA} \quad (6)$$

where  $z$  is the distance from the laser focal plane,  $\theta$  is the half-convergence angle of laser beam coming into the focus,  $M^2$  is the laser quality factor,  $\lambda$  is the laser wavelength, and  $NA$  is the numerical aperture of an objective lens. At each point in time during the pulse duration, the spatial distribution of the laser intensity is described by Eq. (5). As the beam propagates into the sample, the width decreases as described by Eq. (6), and at some point, the laser intensity is absorbed at various locations forming a plasma when it reaches the intensity threshold,  $I_{th}$ , of the material given by [22]

$$I_{th} = \left( \frac{n_c}{n_a \tau_{rec} \beta_{mpi}} \right)^{1/n_{ph}} \quad (7)$$

where  $n_c$  is the electron critical density,  $n_a$  is the density of neutral atoms,  $\beta_{mpi}$  is the field ionization coefficient, and  $n_{ph}$  is the number of absorbed photons. The breakdown will start closest to the focal plane and move upward along the beam axis during the first half of the pulse duration due to the Gaussian temporal distribution of the laser power. This requires a smaller beam spot to reach the threshold intensity at lower powers and a larger beam spot at higher powers. The absorption volume is determined by combining all of the points where absorption occurred during the first half of the laser pulse. The energy in the second half of pulse duration will be absorbed in this absorption volume to generate a higher-density plasma in the absorption volume.

**2.3 Fracture Strength of the Weld Seam.** The material in transmission welded region possesses properties different from that in the initial state. Nanindentation is a nondestructive test capable of extracting elastic modulus and hardness of the specimen, and in addition to those properties, it is widely accepted that  $K_{IC}$  can also be obtained by measuring the postindentation radial crack size emanating from the indent as a function of load as shown by Lawn:  $K_{IC} = k\left(\frac{E}{H}\right)^{1/2} \frac{P}{c^{3/2}}$  [23]. For triangular pyramid indenters such as a Berkovich or cube corner, the profile of the radial crack is more likely a semi-elliptical geometry [24] rather

than halfpenny shape observed for Vicker indenters. For an elliptical crack embedded in an infinite body in tension, Irwin [25] derived the stress intensity factor,  $K_I$ , using 3D potential functions as

$$K_I = \frac{\sigma\sqrt{\pi b}}{E(k)} \left\{ \sin^2 \theta + \frac{b^2}{a^2} \cos^2 \theta \right\}^{1/4} \quad (8)$$

where  $\sigma$  is the tensile stress,  $a$  and  $b$  are major and minor radii of an elliptical crack,  $\theta$  is the angle from the major axis, and  $E(k)$  is a complete elliptic integral of the second kind defined as

$$E(k) = \int_0^{\pi/2} \sqrt{1 - k^2 \sin^2 \varphi} d\varphi; \quad k = \sqrt{1 - b^2/a^2} \quad (9)$$

Although no closed-form solution is available for semi-elliptical surface cracks, proper numerical factors can be used to account for the effect of free surfaces. The free surface factor tends to 1.1215 for long surface cracks, and would tend to 1 for semicircular shapes. The free surface factor,  $f$ , is typically written as [26]

$$f = 1 + 0.1215 \left( 1 - \frac{b}{a} \right) \quad (10)$$

Indentation testing at high loads will initiate radial cracks with known length,  $c$ , from the center of indentation point and with depth,  $d$ , assumed equal to the indentation depth. Therefore, assuming a semi-elliptical geometry with one free surface, the stress intensity factor at the tips of the postindentation radial cracks under an applied tensile stress will be the following:

$$K_I = \frac{\sigma}{E(k)} \sqrt{\frac{\pi c}{2}} r f; \quad r = \frac{b}{a} = \frac{d}{c/2} \quad (11)$$

where  $r$  is depth-to-length ratio of surface semi-elliptical cracks induced by a Berkovich indenter. Depending on the application, the weld seams may be subjected to different types of loading such as tension, shear, etc. Mode I (opening mode) fracture is the most applicable to glasses since they generally fail in tension. From the postindentation radial crack, if the material is under a tensile load, fracture will occur when the stress intensity factor at the crack tip,  $K_I$ , reaches the critical stress intensity factor,  $K_{IC}$ , which is a physical characteristic of the material. Using a power series to express the  $E(k)$  function in Eq. (12) and accounting for only the first four terms, the tensile fracture stress,  $\sigma_f$ , of the materials can be obtained using Eq. (13)

$$E(k) = \frac{\pi}{2} \sum_{n=0}^{\infty} \left[ \frac{(2n)!}{2^{2n} n!^2} \right]^2 \frac{k^{2n}}{1 - 2n} \quad (12)$$

$$\sigma_f = \frac{K_{IC} \sqrt{\pi} [175/256 + 103r^2/256 - 27r^4/256 + 5r^6/256]}{2\sqrt{cr} [1 + 0.1215(1 - r)]} \quad (13)$$

where  $K_{IC}$  is the fracture toughness from indentation. Due to the presence of the crack, the residual strength of the structure decreases progressively with increasing crack size.

### 3 Experimental Setup and Characterization

Transmission welding is performed using a chirped amplified Ti:Sapphire laser system which outputs high energy ultrashort pulses with 800 nm wavelength and 130 fs pulse duration at a 1 kHz repetition rate. Commercial grade borosilicate glass (BK7) 1.0 mm thick was sectioned into 6 mm × 12 mm samples and cleaned by RCA-cleaning [27], and were subsequently pressed together at a pressure of roughly 2 MPa for 10 min. The pressed samples were super glued on the both ends before being fixed to a

motorized linear stage and processed by femtosecond laser pulses. The laser beam was focused by a 40× objective lens with a NA of 0.60 at the interface between the plates. A schematic diagram of the experimental setup is illustrated in Fig. 1.

After the femtosecond laser treatment, the samples were then ground with carbide papers and polished with cerium-oxide and a leather polishing pad to have smooth surface. Reflective light differential interference contrast (DIC) optical microscopy, which can reveal more contrast and details in the feature morphology, was used to obtain the cross section view of the weld seams. The weld zone was examined via nanoindentation using a three-sided Berkovich indenter tip to characterize the mechanical properties. Arrays of 100 nm deep nanoindents with 3 μm spacing in the x- and z-directions were conducted to cover the cross section of both the weld zone and nearby unaffected regions to provide a spatially resolved measurement of material properties. 150 gf–350 gf load nanoindents were also performed on the features to induce cracks in order to investigate the fracture toughness of the weld zones. Different laser pulse energy conditions were used to investigate the effects of laser pulse energy on morphology and mechanical properties of the weld seams.

## 4 Results and Discussion

**4.1 Weld Formation and Geometry.** While other studies [6–8] have used high precision flatness glass plates and required the gap between the plates to be less than  $\lambda/4$  in order that the welding to succeed, BK7 glass plates with standard flatness of 3–5 waves/inch were used in this study. Figure 2 shows the transmission welded cross section (xz-plane) of two BK7 glass plates with the processing condition of 10 μJ laser pulse energy and 0.02 mm/s laser scanning speed from reflective DIC optical microscopy. There is continuity of the material from the top piece to the bottom piece in the processed region. From this figure, it can also be observed that the shape of the affected region is a teardrop shape and it looks similar to the morphology of femtosecond laser modified regions inside a single-piece of a material [11]. AFM topography was also carried out to image cross section profiles across both welded and reference regions as shown in Figs. 3(a)

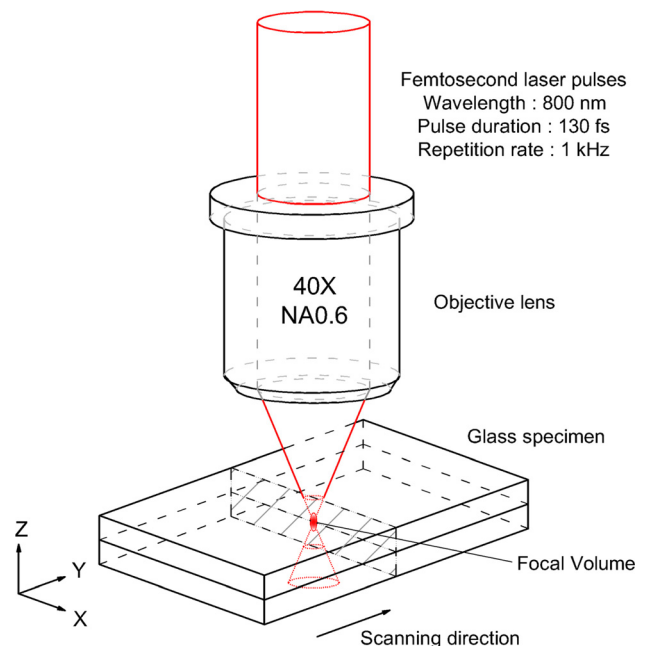


**Fig. 1 Schematic illustration of experimental setup. The laser beam is focused onto the interface of two borosilicate glass plates, and the scanning direction is along the y-axis.**

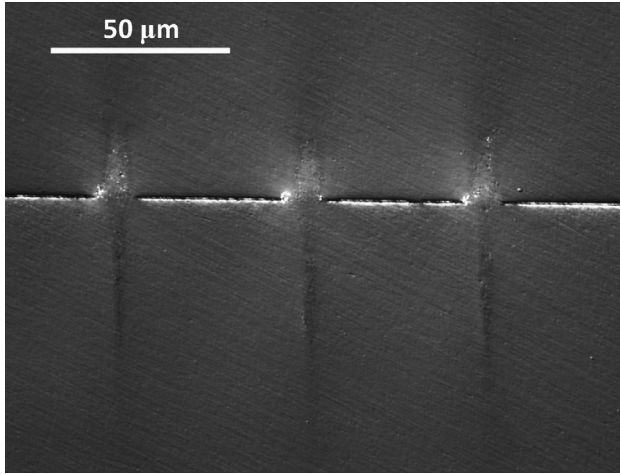


**Fig. 2** Reflective DIC optical microscopy of cross section view (xz-plane) of a weld seam (laser pulse energy of  $10\ \mu\text{J}$ , scanning speed of  $0.02\ \text{mm/s}$ , and repetition rate of  $1\ \text{kHz}$ )

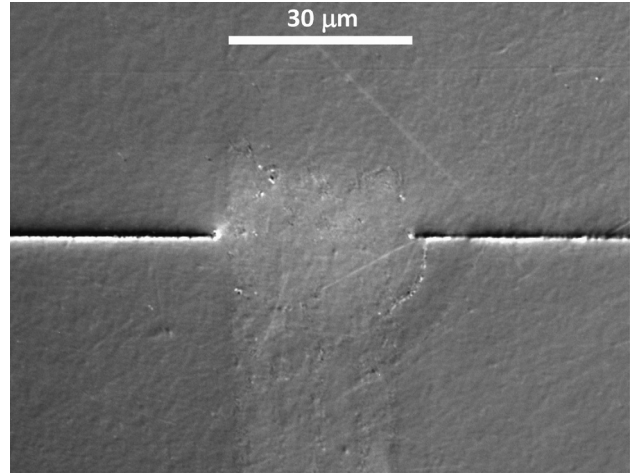
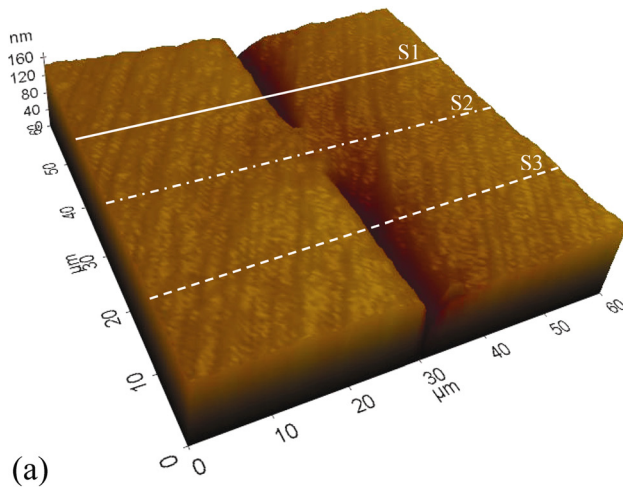
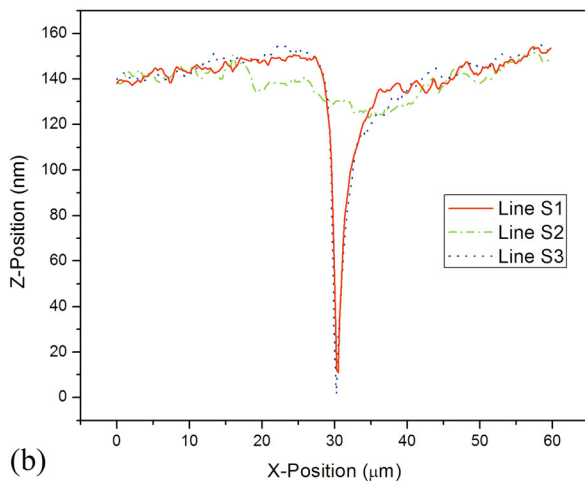


**Fig. 4** Reflective DIC optical microscopy of cross section view (xz-plane) of a multiple-line weld seam (laser pulse energy of  $10\ \mu\text{J}$ , scanning speed of  $0.02\ \text{mm/s}$ , and repetition rate of  $1\ \text{kHz}$ , 5 scanning lines with  $6\ \mu\text{m}$  spacing between lines)



(a)



(b)

**Fig. 3** (a) 3D AFM topography on the cross section (xz-plane) of a weld seam (laser pulse energy of  $10\ \mu\text{J}$  and scanning speed of  $0.02\ \text{mm/s}$ ) and (b) AFM line profiles across glass interface near and on the weld seam

and 3(b). Although the gap between the plates is not as low as  $\lambda/4$  due to the standard flatness of the plates, it is very clear that the two borosilicate glass plates were joined. In order to investigate the possibility of connecting multiple weld lines to have a larger

weld seam, transmission welding of multiple laser scanning lines with the spacing between lines less than the weld width from the single-line case was performed. Figure 4 shows the cross section view (xz-plane) of a sample processed with five overlapping weld lines. The individual weld lines cannot be distinguished, and it can be concluded that the transmission welding of large areas may be performed by automatically controlling the movement of a positioning stage and overlapping welds with a spacing less than the width of a single-line weld seam.

Due to its low repetition rate and the presence of an air gap at the interface, the pressure evolution inside the absorption volume will play an important role in the mechanism of weld seam formation. The glass and air inside the absorption volume that are ionized and experience high temperatures and high pressures will eventually be transformed and solidified, and become the weld joint and surrounding affected regions. According to the numerical analysis of the absorption volume in Sec. 2.2, when a  $10\ \mu\text{J}$  pulse energy is used, the absorption volume is approximately  $9.08 \times 10^{-16}\ \text{m}^3$ , and the surface area of this absorption volume is approximately  $4.80 \times 10^{-10}\ \text{m}^2$ . An average pressure of  $11.0\ \text{GPa}$ , which calculated from Eq. (1), is assumed to be generated inside the absorption volume. From Eq. (3), this pressure causes deflection of the plates in the z-direction of roughly  $44\ \text{nm}$  if the weld line is  $1\ \text{mm}$  from a glue-supported end or  $476\ \text{nm}$  if the weld line is located at the center of the workpiece. The standard roughness of the glass plates and the images in Figs. 2–4 suggest that the final gap at the weld interface is approximately  $2\ \mu\text{m}$ . Assuming the initial gap is less than  $2\ \mu\text{m}$ , due to the effect of laser energy deposition, the gap will be opened wider, and the surface area of the absorption volume will be almost completely confined by the surround solid material with approximately 10% of the area exposed to the open space within the gap. Therefore, depending on the average pressure and the area which is exposed to open space, some fraction of the postshock state material could be driven out of the absorption volume to the surrounding area at the interface between the plates as debris.

To verify this mechanism, the top view (xy-plane) of weld lines processed with different pulse energies as shown in Fig. 5(a), were analyzed. From the numerical analysis in Sec. 2.2, the absorption volume and the deposited energy density increase at a higher rate than laser pulse energy; therefore, as defined by Eq. (1), the average pressure inside the absorption volume decreases with increasing laser pulse energy. Due to higher average pressure and higher deposited energy, debris which was driven out to the area surrounding the welding lines is clearly observed in the two conditions on the right of Fig. 5(a) using lower pulse energy  $10\ \mu\text{J}$

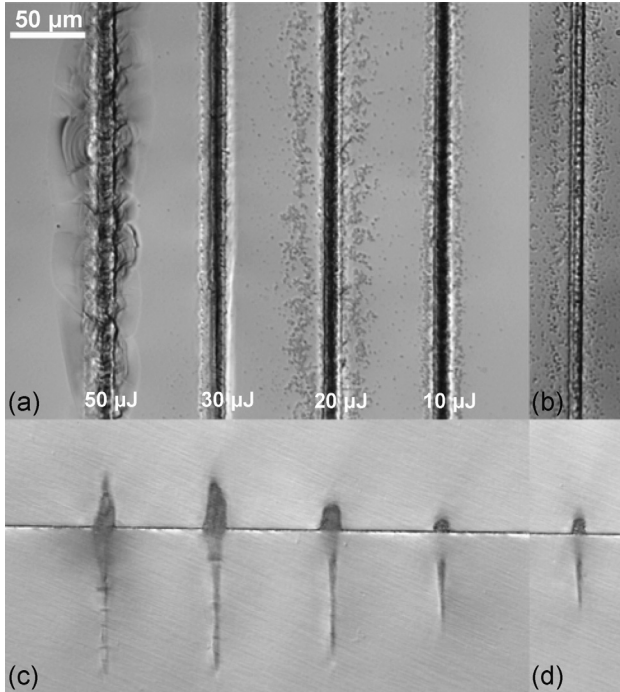


**Fig. 5** (a) Top view (*xy*-plane) and (c) cross section view (*xz*-plane) of weld seams performed at different processing conditions obtained through transmission DIC optical microscopy (laser scanning speed of 0.06 mm/s, 0.04 mm/s, 0.03 mm/s, and 0.02 mm/s, respectively, from the left) (b) Top view (*xy*-plane) and (d) cross section view (*xz*-plane) of a weld seam for 10  $\mu$ J and 0.02 mm/s condition

and 20  $\mu$ J, respectively. This debris is considered to be due to the occurrence of phase explosion under these conditions. However, for the 10  $\mu$ J pulse energy condition the debris was not driven far away from the welding line compared to the 20  $\mu$ J pulse energy, as seen in Fig. 5(a). This could be due to the location of absorption volume with respect to an interface as shown in Fig. 5(c). Because of its teardrop shape, the higher position of the absorption volume with respect to the interface causes the larger confined area of the absorption volume by the surrounding material, and it implies that the shockwave pressure will be greater. Therefore, if the absorption volume is moved up as shown in Fig. 5(d), the debris will be driven further from the welding line as observed in its corresponding top view in Fig. 5(b). On the other hand, no debris will be observed as shown in the two conditions on the left of Fig. 5(a) using pulse energy of 50  $\mu$ J and 30  $\mu$ J, respectively, due to their lower average pressure and lower deposited energy density, which could not induce phase explosion. While significant cracking is observed around the leftmost weld line, this cracking is considered to be due to thermal shock rather than pressure created by the expanding plasma. The higher peak power and higher scanning speed result in a higher peak temperature and greater thermal gradient surrounding the absorption volume, respectively. The thermal stress overcomes the fracture stress of the material, and cracks are initiated as clearly observed in the leftmost weld line of Fig. 5(a).

The effect of laser pulse energy on the weld width is shown in Fig. 6. The weld width should be the same order of magnitude as the width of features created inside single-piece specimen. Higher laser pulse energies have shown to result in larger widths of features in single-piece specimen [11]; therefore, it is expected that the weld width will increase in size when the laser pulse energy is increased as clearly seen in Fig. 6.

**4.2 Absorption Volume Modeling.** To model the absorption volume shape, one should consider both temporal and spatial

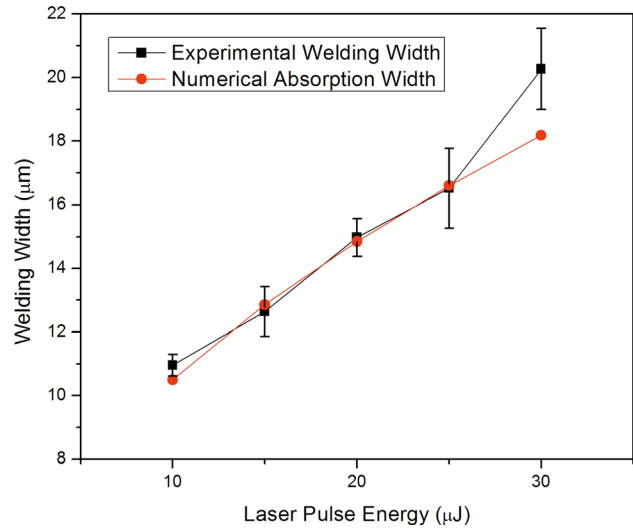


**Fig. 6** Comparison of experimental weld width and simulated absorption width at different laser pulse energies. Error bars denote standard deviation.

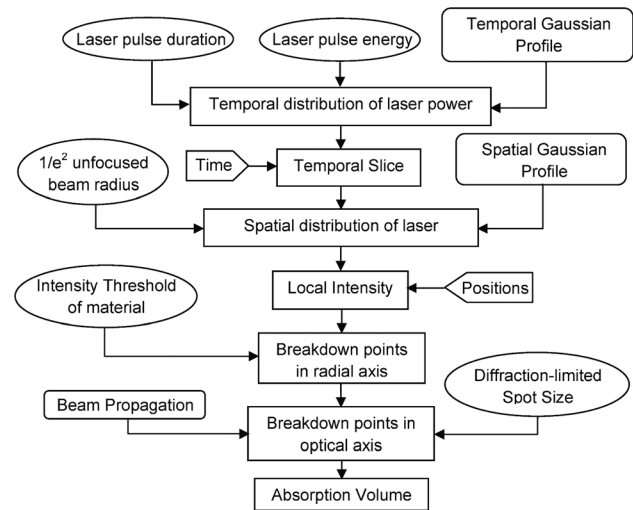


**Fig. 7** Schematic diagram of absorption volume modeling process

distribution characteristics of femtosecond laser pulses, and also account for the focusing characteristics of a collimated laser beam through transparent materials. In a transparent material, significant absorption is not achieved below a specific intensity threshold. This model aims to determine the locations within the material that achieve this intensity as a function of time within the laser pulse duration. Figure 7 illustrates the schematic flow diagram of the absorption volume modeling. From the laser pulse energy, the full-width-at-half-maximum (FWHM) pulse width, and the assumption of a Gaussian temporal profile, the distribution of power in the laser pulse duration can be determined by Eq. (4). Subsequently, using Eq. (5), the distribution of intensity in the unfocused laser spot can be calculated at each point in time during the pulse duration using the  $1/e^2$  radius of the unfocused beam and the assumption of a Gaussian spatial profile. From the laser intensity at any location within the unfocused laser beam and the intensity threshold of the transparent material, the material breakdown locations in the lateral direction of the converging laser beam can be derived by considering how small the beam area should be in order that the intensity at these locations will reach the material intensity threshold. Consequently, the material

breakdown locations along the optical axis can be determined using the diffraction-limited spot size and the beam propagation equation as described by Eq. (6). The material breakdown locations at each point in time form concave-down parabolic line which, when combined over the full temporal profile, form the absorption volume as shown in Figs. 8(a) and 9(a). The numerical calculations have been performed by using parameters presented in Table 1. Assuming a small air gap at the interface, and ignoring reflections at the interface, this model is applicable for transmission welding as well as for processing inside bulk samples.

Figure 8(a) shows the simulated cross sections of the absorption volume at different laser pulse energies. The cross section shape of the absorption volume indeed looks like the teardrop shape. The width and height of cross section increase with increasing laser pulse energy corresponding to experimental results reported in other studies [11–13]. Higher laser pulse energy leads to higher peak power, which generates higher local intensities at the same spot size. Consequently, the material breakdown locations will be farther from the center in the radial axis and will also be farther from the focal plane in the optical axis. Therefore, the height and width of the absorption volume for high laser pulse energies are greater than for low laser pulse energies as shown in Fig. 8(b). The aspect ratios of the absorption volumes at different laser pulse

energies are more-or-less constant; a similar trend was observed for features created in single-piece specimen in a previous study [11]. This trend agrees well with the focal volume aspect ratio calculated using the illumination point spread function, for which the ratio is constant and independent of laser pulse energy [28]. The widths of absorption volume at different laser pulse energies were also compared to the experimental weld widths in Fig. 6. The simulated widths showed good agreement with the experimental ones, and followed the same trend of increasing width for higher laser pulse energy. Therefore, the absorption volume model allows for prediction of the weld width for a wide range of pulse energies.

Figure 9(a) shows the simulated cross sections of the absorption volume using different numerical aperture (NA) objective lenses for a fixed laser pulse energy. For high NAs, the teardrop shape of the absorption volume tends to have more-or-less equivalent size in height and width corresponding to the experimental results of Schaffer et al. [12]. Each point within the Gaussian intensity distribution of the unfocused laser beam requires a specific magnification to reach the intensity threshold of the material. This magnification defines the radius of the focused beam at which absorption will occur and is dependent of the NA of the objective lens. Therefore, the widths of absorption volumes are constant

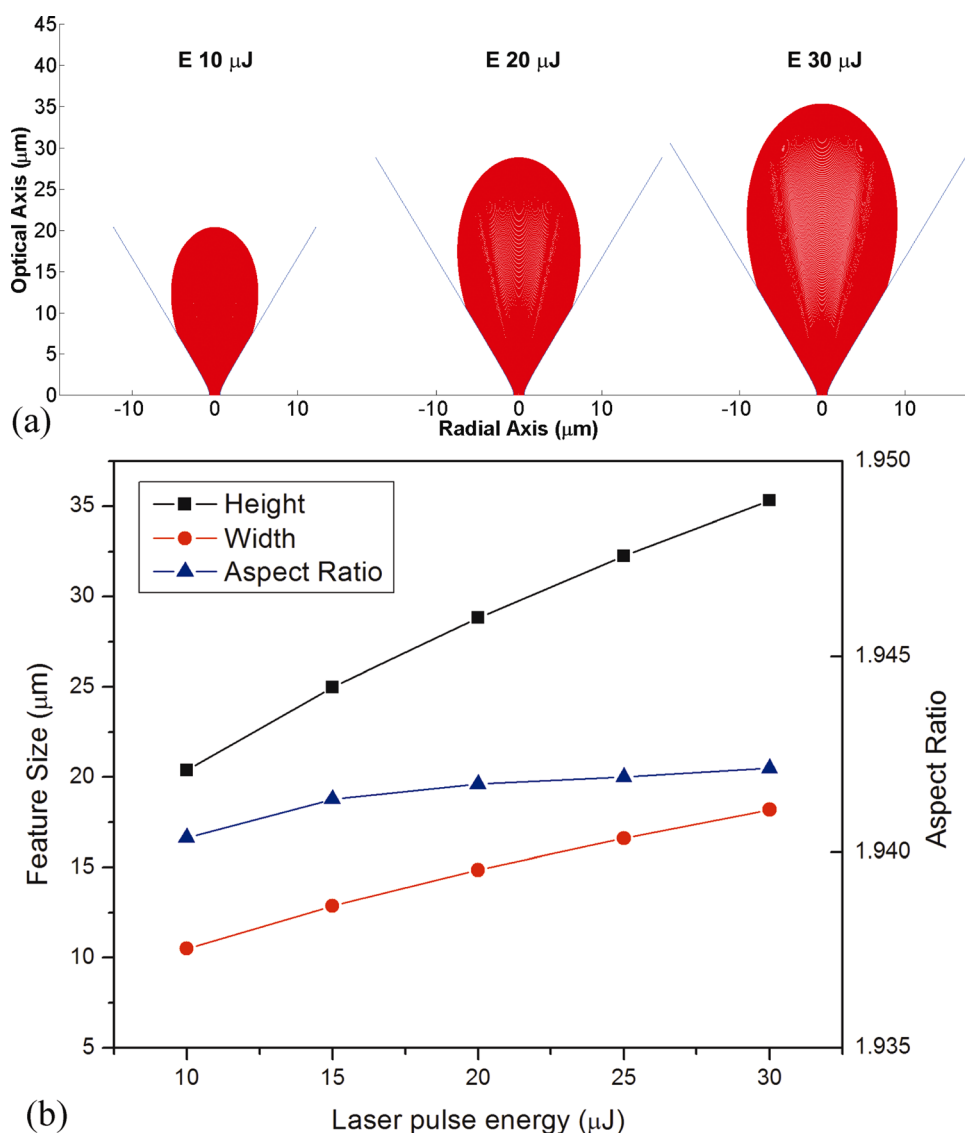


Fig. 8 (a) Cross section view (b) height, width, and height/width ratio of modeling absorption volume at different laser pulse energies (NA 0.6)

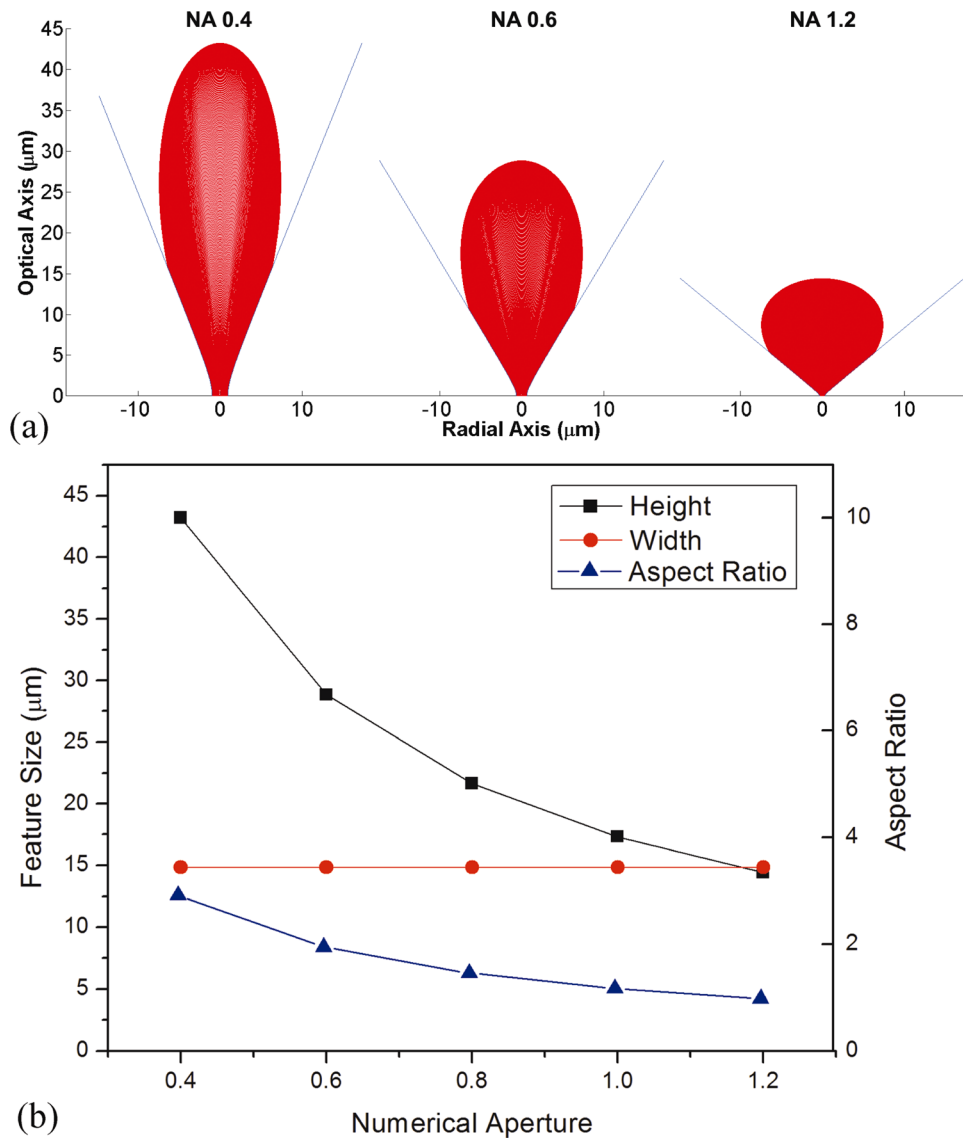


Fig. 9 (a) Cross section view (b) height, width, and height/width ratio of modeling absorption volume at different NAs (laser pulse energy of  $20 \mu\text{J}$ )

Table 1 Laser, optical, and material parameters used in the absorption volume model

Parameters	Value	Unit
Laser wavelength, $\lambda$	800	nm
Laser pulse duration, $t_p$	130	fs
Laser quality factor, $M^2$	1.5	—
Laser pulse energy, $E_p$	10–30	$\mu\text{J}$
Unfocused beam radius, $R_0$	6	mm
Absorption coefficient, $A$	0.7	—
Numerical aperture, $NA$	0.4–1.2	—
Intensity threshold of BK7, $I_{th}$	$2.15 \times 10^{13}$	$\text{W}/\text{cm}^2$

and independent of NA as shown in Fig. 9(b). However, the corresponding breakdown locations of the material along the optical axis depend on the diffraction-limited spot size and the converging angle of the focused laser beam. For higher NAs, the unfocused laser beam is converged at a greater rate; therefore the focused beam will achieve the required magnification and radius at a location closer to the focal plane along the optical axis. The heights of the absorption volumes are thus decreased with higher NAs as shown in Fig. 9(b). The aspect ratio of the absorption

volume decreases with higher NAs, which corresponds well with the feature aspect ratio of the experimental results studied by Schaffer et al. [12].

As seen in Sec. 4.1, the weld width depends on the laser pulse energy. The higher the energy, the wider the weld width; the height of the affected region also increases with laser pulse energy. However, minimizing the size of the region affected by transmission welding may be required for certain applications since there is less alteration of material properties. It can be seen from the numerical model that the higher the numerical aperture, the smaller the aspect ratio and height of absorption volume. Therefore, the absorption volume model could be used to choose the optimal optical and laser processing parameters that should be used in order to get a desirable weld shape. The initial results suggest that higher laser pulse energies and higher numerical apertures are more desirable for transmission welding due to their wider weld widths and smaller affected regions.

**4.3 Mechanical Properties of the Weld.** Figure 10 shows the reflective DIC optical image of a nanoindentation array on the cross section (xz-plane) of a transmission welded line of two borosilicate glass plates. The indents were performed to a depth of 100 nm with a spatial resolution of  $3 \mu\text{m}$  and covered both the

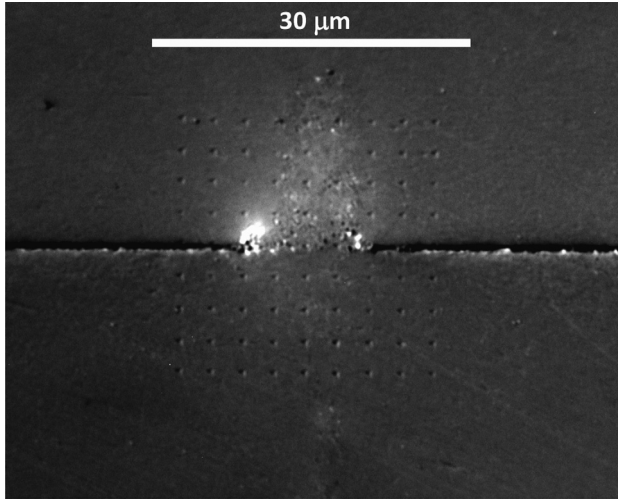


**Fig. 10 Reflective DIC optical image of spatially resolved nanoindentation array (100 nm deep indents with 3  $\mu\text{m}$  spacing) on the cross section (xz-plane) of a weld seam (laser pulse energy of 10  $\mu\text{J}$  and scanning speed of 0.02 mm/s)**

unaffected and welded regions. At same maximum indentation depth, the maximum load of an indent performed in the unaffected region is greater, and its residual depth is shallower than in the welded region, which implies that the mechanical properties in transmission welded region are changed through processing. In order to understand how mechanical properties change, and how they relate to the weld strength, the spatially resolved nanoindentation and indentation fracture will be drawn into consideration.

Figures 11(a) and 11(b) illustrate the contour plots of Young's modulus to hardness (E/H) ratios corresponding to the array of 100 nm deep nanoindents with 3  $\mu\text{m}$  spacing on the cross section (xz-plane) of a transmission welded region and on the cross section of a feature inside a single-piece bulk specimen irradiated by the same laser pulse energy of 10  $\mu\text{J}$ , respectively. The thick white lines in Fig. 11(a) represent the weld interface. Compared to their original values, the E/H ratios in the welded and treated regions are also similar; however, the E/H ratios in the weld seam show two separate regions with high E/H ratios. Figure 12(a) shows the variation of E/H ratios along the three horizontal lines (H<sub>1</sub>–H<sub>3</sub>) across the weld seam of Fig. 11(a). The vertical dashed-dotted line in this figure represents the optical axis, which is the line in z-direction that passes through the center of the weld seam. Due to the effect of the air gap at the interface, some fraction of laser energy may be reflected back to the top piece, and an air gap with a lower breakdown threshold may be ionized during irradiation and partially obstruct the nonlinear absorption of laser beam in the bottom piece of material. Therefore, less energy is coupled into the bottom portion of the absorption volume, and there is less change in mechanical properties in the region of the weld seam right below the interface as shown by the smaller increase in E/H ratios in line H<sub>3</sub> compared to lines H<sub>1</sub> and H<sub>2</sub> in Fig. 12(a). The E/H ratios along the line C1 across the weld seam do not change gradually as in the case of the one-piece specimen shown by line C2 in Fig. 12(b). Therefore, the air gap plays a significant role in the coupling of laser energy into the bottom piece during transmission welding.

From indentation analysis, higher E/H corresponds to a higher residual stress field intensity, implying a weaker elastic recovery and thus less pronounced radial crack extension during the unloading half-cycle [23]. Therefore, the E/H ratio of a material can be directly related to the fracture toughness of material, and higher E/H ratios may lead to higher fracture toughness. To confirm this effect in the transmission welded region, deeper indents were performed to induce radial cracks at the corners of the

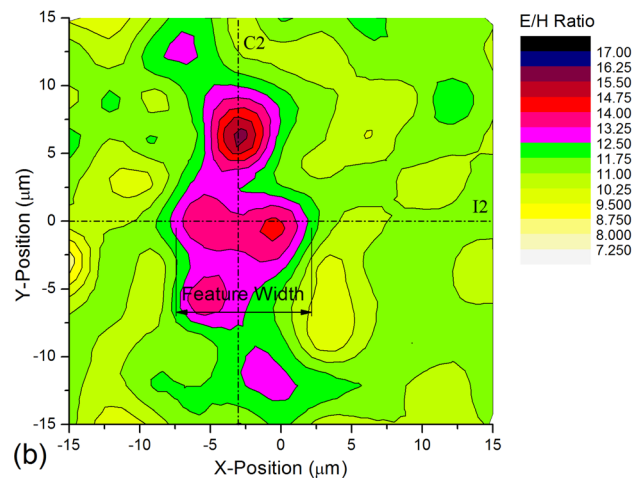
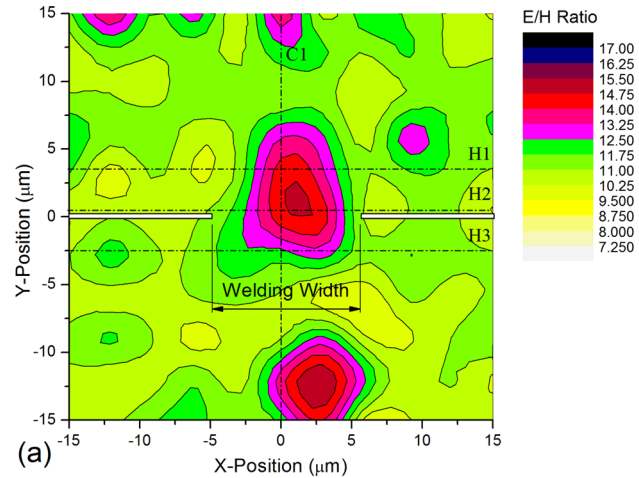
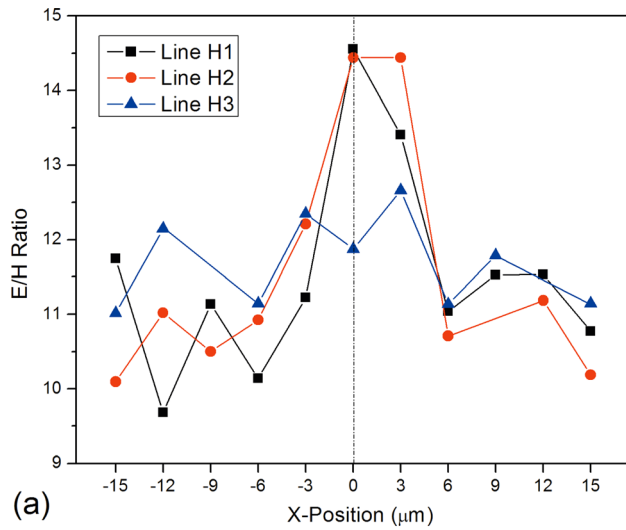


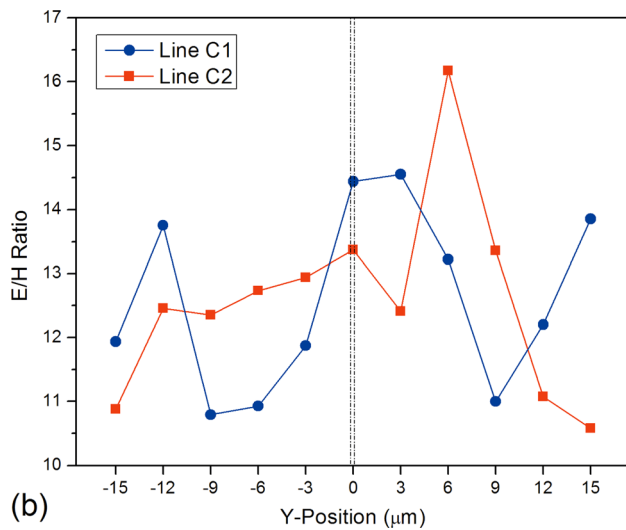
**Fig. 11 Spatially resolved determination of the ratio between Young's modulus and hardness (E/H) on the cross section of (a) a welded region of two-piece specimen (b) a feature inside one-piece specimen using the same laser pulse energy of 10  $\mu\text{J}$  and scanning speed of 0.02 mm/s. The contour maps correspond to the array of 100 nm depth nanoindents with 3  $\mu\text{m}$  spacing.**

nanoindentation features. Figure 13 shows a DIC optical image of cracks induced by a high load nanoindentation test. The bottom corner of the nanoindentation imprint is within the welded region, and the crack at the bottom corner extends across the weld at the interface between the two borosilicate glass plates. Comparing the crack lengths at the three corners of the nanoindentation imprint in Fig. 13, it is clear that the crack length in the welded region is shorter than those in unaffected region. Due to higher E/H ratio and shorter crack length in the transmission welded region, it can be confirmed that the fracture toughness of material inside the welded region is increased which agrees with the fracture toughness increase observed in ultrafast laser-treated areas of glasses obtained using double torsion tests by Borrelli et al. [9]. The direction of a propagating crack front can be altered by a residual stress field and since there are significant residual stresses in glasses irradiated by femtosecond lasers [29,30], the crack will be on a more tortuous path, and thus, more energy will be required for propagation [31].

Figure 14 shows the indentation fracture toughness of material inside the weld seam compared to the reference material, and also shows the effect of laser pulse energy on the fracture toughness. In the ultrafast laser-treated region, there are more nonbridging oxygen hole centers (NBOHCs) [32] and the connectivity of the structure is decreased, and at the same time the remaining



(a)



(b)

**Fig. 12** The variation of E/H ratio (b) versus X-position along the horizontal lines (lines H1–H3) in Fig. 11(a) across the weld seam (b) versus Y-position along the line C1 in Fig. 11(a) across the weld seam and the line C2 in Fig. 11(b) across the feature inside one-piece specimen (laser pulse energy of  $10 \mu\text{J}$ , scanning speed of  $0.02 \text{ mm/s}$ )

connected ring structures of material become more compact [11]. The presence of NBOHCs may help branch the main crack while a higher driving force is required to propagate the main crack through the more compact ring structure. Therefore, the fracture toughness of material in the weld seam is greater than in the reference material as shown in Fig. 14. The higher the laser pulse energy, the stronger the laser-matter interaction is inside the focal volume. It has been shown that there are more NBOHCs and more compact ring structures when processing is performed using higher pulse energies [32]. The presence of micro cracks, which are initially observed in the  $30 \mu\text{J}$  case and very distinctive in the  $50 \mu\text{J}$  case, has been shown in Fig. 5. Each of these micro cracks is a fracture surface which aids crack propagation, reducing the toughness of the material [31]. Therefore, there is an increasing trend in fracture toughness with pulse energy in the energy range of  $10\text{--}25 \mu\text{J}$  and the fracture toughness begins decreasing at a pulse energy of  $30 \mu\text{J}$  as shown in Fig. 14. It is also shown that in case of indentation field cover the area of the nonhomogenous material (weld seam plus reference region), the fracture toughness calculated by nanoindentation method will be varied depending on the size of indentation filed. The higher the indentation field could affect the variation in fracture toughness as seen in Fig. 14.

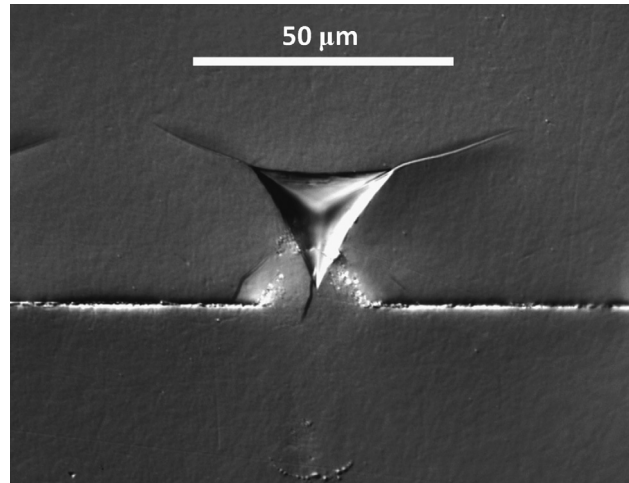


**Fig. 13** Reflective DIC optical microscopy of indentation fracture on cross section (xz-plane) of a weld seam (laser pulse energy of  $30 \mu\text{J}$ , scanning speed of  $0.02 \text{ mm/s}$ , repetition rate of  $1 \text{ kHz}$ )

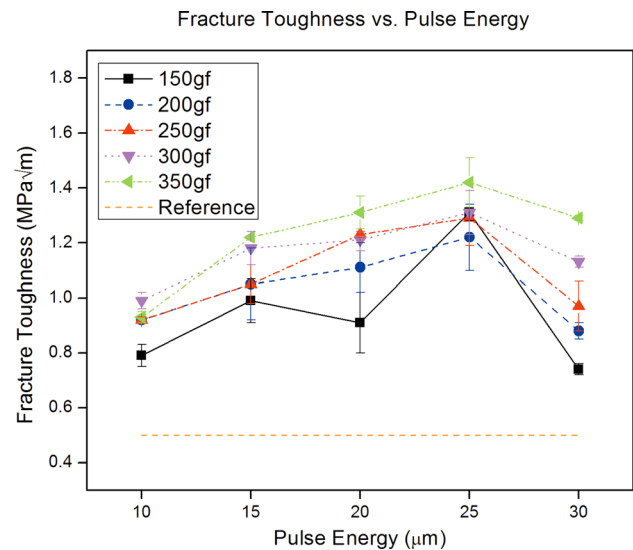


**Fig. 14** Fracture Toughness of the material in welded regions with different laser pulse energy levels ( $10 \mu\text{J}$ – $30 \mu\text{J}$ ) at fixed laser scanning speed of  $0.02 \text{ mm/s}$  and in a reference region from indentation fracture measurements at different loads. Error bars denote standard deviation.

Indentation at different levels of load will produce cracks with different lengths at the corners of indentation imprint. Assuming that these cracks have a semi-elliptical geometry, the externally applied tensile stress to fracture the material both in the weld seam and the reference regions can be calculated by Eq. (13). The fracture stress of a cracked plate is lower than both the strength of the uncracked material and the ultimate tensile strength. When the tensile fracture strength of materials is plotted as a function of crack length the material with higher fracture toughness will show higher residual strength [33]. Figure 15 shows the tensile fracture stress of material in the reference and welded regions as a function of initial crack length. Due to the higher fracture strength at the same crack length, for a given crack size, the tensile stress required to fracture the weld seam is higher than the reference material. To obtain high fracture energy, it is necessary for glass to utilize energy absorbing processes [34]. It has been shown that several processes can toughen glass resulting in an energy absorbing process around the primary crack front and nonlinear behavior

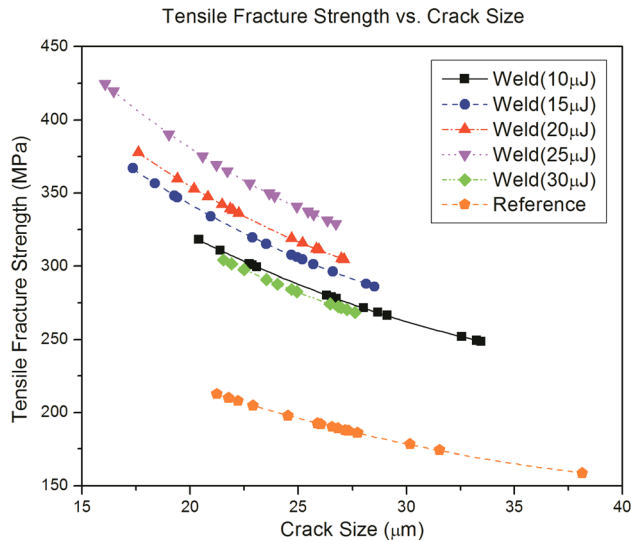


**Fig. 15 Fracture Strength as a function of crack size of the material in welded regions with different laser pulse energy levels (10  $\mu$ J–30  $\mu$ J) at fixed laser scanning speed of 0.02 mm/s and in a reference region**

prior to fracture [31]. The ultrafast laser-treated region, including the weld seam, could be analogous to a toughened processed zone; therefore, a higher stress is required to fracture the weld compared to the reference regions. This is consistent with concepts that suggest that toughening (increase  $K_{IC}$ ) leads to strengthening (increase  $\sigma_f$ ) especially for brittle solids such as glass [35]. The effect of the laser pulse energy on the fracture strength is also illustrated in Fig. 15. Due to the presence of micro cracks at sufficiently higher laser pulse energies as mentioned earlier in this section, it can be seen that the fracture strength does not monotonically increase with laser pulse energy, rather there is an optimum pulse energy beyond which the resultant fracture strength will decrease. However, the detrimental effect of the micro cracks is smaller than the beneficial effect of the compact ring structure (three-member rings) which has the highest barrier to fracture of all ring configurations [36]; therefore, the fracture strengths in welded regions for all laser pulse energy conditions in this study are still higher than the reference region.

## 5 Conclusion

Transmission welding of two borosilicate glass plates with standard flatness was performed by using low repetition rate femtosecond laser irradiation. The weld cross section (xz-plane) revealed that the transmission welding of standard flatness glass plates was successful. The weld morphology was investigated, and it was observed that the affected region is a teardrop shape similar to the features created by femtosecond laser irradiation of the interior of single-piece transparent samples. Large area transmission welding seams can also be formed by applying a multiple-line overlap welding process. A numerical model was developed to investigate the size and shape of the absorption volume as a function of laser pulse energy and numerical aperture of the objective lens. The model was able to predict the teardrop shape of the absorption volume, and the width of the absorption volume agreed well with the weld widths obtained through experiments for a wide range of pulse energies. The E/H ratios in the weld seam showed two separate regions with high E/H ratios implying that air gap plays a significant role in the coupling of laser energy into the bottom piece during transmission welding. The material inside the welded region revealed an increase in fracture toughness; therefore, a higher stress may be required to fracture the weld compared to the reference region. The geometry and mechanical properties of the weld seam obtained in this study

suggest that transmission welding using low repetition rate femtosecond laser irradiation is a promising technique for spatially selective joining of glasses.

## Acknowledgment

This work is partially supported under NSF Grant No.: CMMI-0936171. Financial support from the Royal Thai government is also gratefully acknowledged. Use of atomic force microscopy equipment in Professor James Hones's laboratory in Columbia University and a nanoindenter in Professor Jeffrey Kysar's laboratory in Columbia University are greatly appreciated.

## References

- [1] Watanabe, W., Onda, S., Tamaki, T., and Itoh, K., 2007, "Joining of Transparent Materials by Femtosecond Laser Pulses," *Proc. SPIE*, **6460**, p. 646017.
- [2] Tamaki, T., Watanabe, W., Nishii, J., and Itoh, K., 2005, "Welding of Transparent Materials Using Femtosecond Laser Pulses," *Jpn J. Appl. Phys.*, **44**(22), pp. L687–L689.
- [3] Watanabe, W., Onda, S., Tamaki, T., Itoh, K., and Nishii, J., 2006, "Space-Selective Laser Joining of Dissimilar Transparent Materials Using Femtosecond Laser Pulses," *Appl. Phys. Lett.*, **89**(2), p. 021106.
- [4] Tamaki, T., Watanabe, W., and Itoh, K., 2006, "Laser Micro-Welding of Transparent Materials by a Localized Heat Accumulation Effect Using a Femtosecond Fiber Laser at 1558 nm," *Opt. Express*, **14**(22), pp. 10460–10468.
- [5] Bovatsek, J., Arai, A., and Schaffer, C. B., 2006, "Three-Dimensional Micro-machining Inside Transparent Materials Using Femtosecond Laser Pulses: New Applications," *CLEO/QELS and PhAST 2006*, CA, pp. 8–9.
- [6] Miyamoto, I., 2007, "Local Melting of Glass Material and Its Application to Direct Fusion Welding by Ps-Laser Pulses," *J. Laser Micro/Nanoeng.*, **2**(1), pp. 7–14.
- [7] Horn, A., Mingareev, I., Werth, A., Kachel, M., and Brenk, U., 2008, "Investigations on Ultrafast Welding of Glass–Glass and Glass–Silicon," *Appl. Phys. A*, **93**(1), pp. 171–175.
- [8] Miyamoto, I., Horn, A., Gottmann, J., Wortmann, D., Mingareev, I., Yoshino, F., Schmidt, M., and Bechtold, P., 2008, "Novel Fusion Welding Technology of Glass Using Ultrashort Pulse Lasers," *Proceedings of 27th International Congress on Applications on Lasers & Electro-Optics*, Temecula, CA, pp. 112–121.
- [9] Borrelli, N., Helfinstine, J., Price, J., and Schroeder, J., 2008, "Glass Strengthening With an Ultrafast Laser," *Proceedings of 27th International Congress on Applications on Lasers & Electro-Optics*, Temecula, CA, pp. 185–189.
- [10] Bellouard, Y., Colomb, T., Depeursinge, C., Dugan, M., Said, A. A., and Bado, P., 2006, "Nanoindentation and Birefringence Measurements on Fused Silica Specimen Exposed to Low-Energy Femtosecond Pulses," *Opt. Express*, **14**(18), pp. 8360–8366.
- [11] Kongsuwan, P., Wang, H., Vukelic, S., and Yao, Y. L., 2010, "Characterization of Morphology and Mechanical Properties of Glass Interior Irradiated by Femtosecond Laser," *J. Manuf. Sci. Eng.*, **132**(4), p. 041009.
- [12] Schaffer, C. B., Jamison, A. O., and Mazur, E., 2004, "Morphology of Femtosecond-Laser-Induced Structural Changes in Bulk Transparent Materials," *Appl. Phys. Lett.*, **84**(9), pp. 1441–1443.
- [13] Miyamoto, I., 2007, "Fusion Welding of Glass Using Femtosecond Laser Pulses With High-repetition Rates," *J. Laser Micro/Nanoeng.*, **2**(1), pp. 57–63.
- [14] Hallo, L., Mézel, C., Bourgeade, A., Hébert, D., Gamaly, E. G., and Juodkazis, S., 2010, "Laser-Matter Interaction in Transparent Materials: Confined Micro-explosion and Jet Formation," *Extreme Photonics & Applications*, T. J. Hall, S. V. Gaponenko, and S. A. Paredes, eds., Springer Netherlands, pp. 121–146.
- [15] Gamaly, E. G., Luther-Davies, B., Hallo, L., Nicolai, P., and Tikhonchuk, V. T., 2006, "Laser-Matter Interaction in the Bulk of a Transparent Solid: Confined Microexplosion and Void Formation," *Phys. Rev. B*, **73**(21), p. 214101.
- [16] Kitchener, J. A., and Prosser, A. P., 1957, "Direct Measurement of the Long-Range van der Waals Forces," *Proc. R. Lond. A*, **242**(1230), pp. 403–409.
- [17] Gere, J. M., and Timoshenko, S. P., 1997, *Mechanics of Materials*, PWS Pub. Co., Boston.
- [18] Sokolowski-Tinten, K., Bialkowski, J., Cavalleri, A., Linde von der, D., Oparin, A., Meyer-ter-Vehn, J., and Anisimov, S., 1998, "Transient States of Matter during Short Pulse Laser Ablation," *Phys. Rev. Lett.*, **81**(1), pp. 224–227.
- [19] Rethfeld, B., Sokolowski-Tinten, K., Linde von der, D., and Anisimov, S. I., 2004, "Timescales in the Response of Materials to Femtosecond Laser Excitation," *Appl. Phys. A*, **79**(4–6), pp. 767–769.
- [20] Zhigilei, L. V., and Garrison, B. J., 2000, "Microscopic Mechanisms of Laser Ablation of Organic Solids in the Thermal and Stress Confinement Irradiation Regimes," *J. Appl. Phys.*, **88**(3), pp. 1281–1298.
- [21] Miotello, A., and Kelly, R., 1999, "Laser-Induced Phase Explosion: New Physical Problems When a Condensed Phase Approaches the Thermodynamic Critical Temperature," *Appl. Phys. A: Mater. Sci. Process.*, **69**(7), pp. S67–S73.
- [22] Hallo, L., Bourgeade, A., Tikhonchuk, V. T., Mezel, C., and Breil, J., 2007, "Model and Numerical Simulations of the Propagation and Absorption of a Short Laser Pulse in a Transparent Dielectric Material: Blast-Wave Launch and Cavity Formation," *Phys. Rev. B*, **76**(2), p. 024101.
- [23] Lawn, B. R., 1993, *Fracture of Brittle Solids*, Cambridge University Press, Cambridge, United Kingdom.

- [24] Kese, K., and Rowcliffe, D. J., 2003, "Nanoindentation Method for Measuring Residual Stress in Brittle Materials," *Mater. Sci.*, **16**, pp. 811–816.
- [25] Irwin, G. R., 1962, "Crack-Extension Force for a Part-Through Crack in a Plate," *J. Appl. Mech.*, **29**(4), pp. 651–654.
- [26] Tada, H., Paris, P. C., and Irwin, G. R., 2000, *The Stress Analysis of Cracks Handbook*, ASME Press, New York.
- [27] Kern, W., 1990, "The Evolution of Silicon Wafer Cleaning Technology," *J. Electrochem. Soc.*, **137**(6), pp. 1887–1892.
- [28] Zipfel, W. R., Williams, R. M., and Webb, W. W., 2003, "Nonlinear Magic: Multiphoton Microscopy in the Biosciences," *Nat. Biotechnol.*, **21**(11), pp. 1369–1377.
- [29] Bhardwaj, V. R., Corkum, P. B., Rayner, D. M., Hnatovsky, C., Simova, E., and Taylor, R. S., 2004, "Stress in Femtosecond-Laser-Written Waveguides in Fused Silica," *Opt. Lett.*, **29**(12), pp. 1312–1314.
- [30] Ye, D., Bing-Kun, Y., Bo, L., Jian-Rong, Q., Xiao-Na, Y., Xiong-Wei, J., and Cong-Shan, Z., 2005, "Thermal Stress-Induced Birefringence in Borate Glass Irradiated by Femtosecond Laser Pulses," *Chin. Phys. Lett.*, **22**(10), pp. 2626–2629.
- [31] Mecholsky, J. J., 1983, "Toughening in Glass Ceramics," *Fracture Mechanics of Ceramics, Volume 6: Measurements, Transformations, and High-Temperature Fracture*, R. C. Bradt, A. G. Evans, D. P. H. Hasselman, and F. F. Lange, eds., Plenum Press, New York.
- [32] Krol, D., 2008, "Femtosecond Laser Modification of Glass," *J. Non-Cryst. Solids*, **354**(2–9), pp. 416–424.
- [33] Broek, D., 1986, *Elementary Engineering Fracture Mechanics*, Martinus Nijhoff Publishers, Dordrecht, The Netherlands.
- [34] Soga, N., 1985, "Elastic Moduli and Fracture Toughness of Glass," *J. Non-Crystal. Solids*, **73**(1–3), pp. 305–313.
- [35] Varshneya, A. K., 1994, *Fundamentals of Inorganic Glasses*, Academic Press, Inc., San Diego, CA.
- [36] West, J., 1999, "The Application of Fractal and Quantum Geometry to Brittle Fracture," *J. Non-Crystal. Solids*, **260**(1–2), pp. 99–108.